JBO Journal of Biomedical Optics

RESEARCH PAPER

Theoretical and experimental study of attenuation in cancellous bone

Wenyi Xu,[a,†] **Weiya Xie**,[a,†] **Dong Yu**,[a] **Haohan Sun**,[a] **Ying Gu**,[a] **Xingliang Tao**,[a] **Menglu Qian**,[a] **Liming Cheng**,[b] **Hao Wang**,[a,*] **and Qian Cheng**[a,c,d,*]

[a]Tongji University, Institute of Acoustics, School of Physics Science and Engineering, Shanghai, China
[b]Tongji University, Key Laboratory of Spine and Spinal Cord Injury Repair and Regeneration of Ministry of Education, Shanghai, China
[c]National Key Laboratory of Autonomous Intelligent Unmanned Systems, Shanghai, China
[d]Frontiers Science Center for Intelligent Autonomous Systems, Ministry of Education, Shanghai, China

ABSTRACT. **Significance:** Photoacoustic (PA) technology shows great potential for bone assessment. However, the PA signals in cancellous bone are complex due to its complex composition and porous structure, making such signals challenging to apply directly in bone analysis.

Aim: We introduce a photoacoustic differential attenuation spectrum (PA-DAS) method to separate the contribution of the acoustic propagation path to the PA signal from that of the source, and theoretically and experimentally investigate the propagation attenuation characteristics of cancellous bone.

Approach: We modified Biot's theory by accounting for the high frequency and viscosity. In parallel with the rabbit osteoporosis model, we build an experimental PA-DAS system featuring an eccentric excitation differential detection mechanism. Moreover, we extract a PA-DAS quantization parameter—slope—to quantify the attenuation of high- and low-frequency components.

Results: The results show that the porosity of cancellous bone can be evaluated by fast longitude wave attenuation at different frequencies and the PA-DAS slope of the osteoporotic group is significantly lower compared with the normal group ($^{**}p < 0.01$).

Conclusions: Findings demonstrate that PA-DAS effectively differentiates osteoporotic bone from healthy bone, facilitating quantitative assessment of bone mineral density, and osteoporosis diagnosis.

Keywords: cancellous bone; high-frequency viscous corrections; Biot's theory; photoacoustic differential attenuation spectrum; acoustic propagation characteristic; osteoporosis

Paper 230317SSRR received Oct. 9, 2023; revised Feb. 16, 2024; accepted Feb. 19, 2024; published Mar. 19, 2024.

1 Introduction

Osteoporosis and fractures stemming from it have emerged as chronic diseases adversely affecting the health of the elderly.[1] As populations age, the annual global increase in the number of fracture patients is ~8.9 million, leading to a considerable rise in public health costs.[2–4]

*Address all correspondence to Qian Cheng, q.cheng@tongji.edu.cn; Hao Wang, wanghao@tongji.edu.cn.

†These authors contributed equally to this paper.

Therefore, early diagnosis of osteoporosis not only can prevent fractures but also substantially reduce healthcare expenditures and resource usage.

Compared to dense bone, the microstructure and chemical composition of cancellous bone are more sensitive to osteoporosis, as evidenced by reduced trabecular thickness, connectivity, and number, along with increased lipid content,[5–8] suggesting that cancellous bone is ideally suited as a diagnostic site for early osteoporosis. However, the unique structural characteristics of cancellous bone make its detection and quantitative evaluation challenging, thereby complicating the early diagnosis of osteoporosis. The primary detection methods employed in clinical and research settings for osteoporosis include dual-energy X-ray absorptiometry (DEXA), quantitative computed tomography (QCT), magnetic resonance imaging (MRI), and quantitative ultrasound (QUS).[9–12] DEXA serves as the "gold standard," primarily because it provides the best predictor of osteoporotic fractures through bone mineral density (BMD) information.[13] However, DEXA accounts for only 60% to 70% of changes in bone strength and lacks information on microstructure and elasticity.[14] QCT extends bone analysis from two to three dimensions, providing both volumetric BMD and microstructural characteristics.[15,16] However, its utility is hampered by radiation hazards and a lack of chemical information. MRI can identify alterations in bone marrow fat content and microstructure, facilitating early diagnosis.[17–19] Nonetheless, its high cost and operational complexity limit its widespread use.[20,21] QUS, being radiation-free, quick, affordable, and user-friendly, has gained traction as a powerful tool for screening bone quality.[5,22,23] Initially centered on cortical bone,[24–26] QUS is increasingly being used to explore cancellous bone characteristics due to its heightened sensitivity to osteoporotic changes. It provides physical information on BMD, bone microstructure, and mechanical properties, mainly by detecting the speed of sound (SoS) and broadband ultrasound (US) attenuation.[12,27] However, it falls short of detecting changes in the organic chemical composition of bone tissue.

Photoacoustic (PA) techniques offer both chemical and physical insights into biological tissues and have been utilized for tissue identification and disease detection, including osteoporosis.[28–32] During the past decade, considerable advancements have been made in PA-based bone evaluation. Mandelis and Lashkari[33] established a set of photoacoustic-ultrasound (PA-US) backscattering detection systems, successfully detecting minute changes in the BMDs of both cancellous and cortical bones. Their study indicated that the apparent integral backscattering coefficient decreases as the collagen content decreases.[34–36] Wang[37,38] employed three-dimensional PA imaging (PAI) and power spectral analysis to achieve both qualitative and quantitative evaluations of bone microstructure. He also introduced multispectral PA decoupling and thermal PA methods for quantitative evaluation of the organic and inorganic chemical components in cancellous bone.[37–39] Additionally, a combined PA-US system was developed, verifying the *in vivo* feasibility of assessing human calcaneus microstructure and chemical composition.[40] Steinberg developed a multispectral PA-US dual-mode system capable of *in vivo* detection of fat and blood ratios in tibial bone marrow.[41] The SoS for the first arriving wave in the tibia showed a strong correlation with the SoS value based on QUS.[42] Feng et al.[43] simulated various aspects of PA in skeletal tissues, including light attenuation and distribution, along with PA signal generation and propagation, based on a three-dimensional model. They proposed a PA physicochemical spectral method for assessing changes in the chemical composition and microstructure of cancellous bone.[44,45] Our group has leveraged the MWPA time-frequency spectral analysis method to evaluate both the chemical content (minerals and lipids) and microstructure of bone tissues, based on the distinct optical absorption characteristics and sizes of various chromophores present.[46,47] The preceding research in this field demonstrates the successful application of various PAI and spectral analysis methods for osteoporosis diagnosis, making it possible to assess BMD, bone microstructure, and chemical composition in a comprehensive manner.[48]

Nevertheless, the intricacy of PA signals, which arise from the two-phase, solid–liquid porous structure of cancellous bone, presents a significant challenge in using PA techniques for imaging of bone marrow distribution in cancellous bone.[49] First, PA signals generated from various chemical clusters within cancellous bone with different microscales have complex optical and ultrasonic spectral distributions. In addition, these chemical clusters have uneven spatial distributions, adding another layer of complexity to the spatial distribution of PA sources.

Thus the PA sources of cancellous bone possess a threefold complexity. Second, as these PA signals navigate through the cancellous bone, they undergo multiple scattering and attenuation events. Therefore, the final PA signal received by the transducers is a composite of broadband signals from distributed PA sources and the acoustic propagation characteristics specific to the porous cancellous bone. Decoupling these signals could yield valuable multidimensional insights into cancellous bone.

In this paper, we do a focused study—both theoretical and experimental—on the high-frequency broadband PA signal propagation generated by bone marrow in cancellous bone. Theoretically, we apply high-frequency and viscous corrections to Biot's theory, tailoring it for bone marrow PA signal propagation in two-phase solid–liquid porous media. The numerical simulations of PA wave modes and velocity and attenuation coefficients are also employed for validation. In the method, we propose a PA differential attenuation spectrum (PA-DAS) method to remove the contribution of PA sources on PA signals in the frequency domain. Subsequently, *ex vivo* experiments are performed to measure PA-DAS, and a quantitative PA-DAS parameter is extracted to evaluate BMD and diagnose osteoporosis. Our results highlight the potential utility of this method for comprehensive bone quality assessment and lay a foundation for the further PAI study of bone marrow distribution in cancellous bone.

2 Modified Biot's Theory

Cancellous bone is a complex porous medium composed of solid trabecular bone interspersed with fluid-filled bone marrow clusters, making it a typical example of a porous, elastic, viscous medium. Biot and Willis[50–55] established the elastic theory for understanding acoustic propagation in such saturated solid–liquid two-phase porous media, thereby enabling further theoretical research in the field. Biot's theory has subsequently found applications in the nondestructive evaluation of bone using biomedical US.[56–62] However, Biot's theory is limited to cases where the acoustic frequency is below the medium's critical frequency f_c, and the flow of liquid through the pores is well-described by Poiseuille flow. The critical frequency f_c is defined as[63]

$$f_c = \frac{\phi\eta}{2\pi\rho_f\mathcal{K}}, \tag{1}$$

where ϕ denotes the porosity, η denotes the fluid viscosity, ρ_f represents the fluid density, and $\mathcal{K}$ denotes the permeability. For cancellous bone filled with viscous bone marrow, f_c is typically in the range of 1 to 10 kHz.[64,65] The sizes of the trabecular bone vary from 50 to 200 μm, while the trabecular spaces (bone marrow clusters) range from 0.2 to 3 mm.[66] The SoS in trabecular bone and bone marrow are 3200 and 1500 m/s, respectively.[67] Notably, the frequencies of PA signals generated in these structures exceed 220 kHz,[68] far surpassing f_c, as we discussed in Appendix A2 in Supplementary Material. This means that the laminar flow condition described by Poiseuille's law no longer holds, necessitating modifications to Biot's theory for high-frequency applications.

In addition, the viscous nature of the fluid bone marrow leads to energy dissipation due to the relative motion between the fluid and the solid trabecular framework, further indicating the need for viscosity corrections. To account for the dissipation of acoustic wave propagation in a solid–liquid two-phase porous medium, the governing equations of motion can be expressed as follows:[54,55]

$$\mu_b\nabla^2\vec{u} + (\lambda_b + \mu_b)\nabla e + Q\nabla\epsilon = \frac{\partial^2}{\partial t^2}(\rho_{11}\vec{u} + \rho_{12}\vec{U}) + b\frac{\partial}{\partial t}(\vec{u} - \vec{U}), \tag{2}$$

$$Q\nabla e + R\nabla\epsilon = \frac{\partial^2}{\partial t^2}(\rho_{12}\vec{u} + \rho_{22}\vec{U}) - b\frac{\partial}{\partial t}(\vec{u} - \vec{U}). \tag{3}$$

where $\vec{u}$ denotes the solid skeleton displacement vector, and $\vec{U}$ represents the liquid displacement vector. The elastic constants μ_b and λ_b characterize the frame's material elasticity and also depend on structural parameters, such as porosity ϕ. R and Q are the additional elastic constants, with Q being Biot's constant that describes the coupling between the liquid and solid phases. $e = e_{11} + e_{22} + e_{33} = \nabla\cdot\vec{u}$ denotes the normal strains for the solid, $\epsilon = \epsilon_{11} + \epsilon_{22} + \epsilon_{33} = \nabla\cdot\vec{U}$

denotes the strain for fluid, whereas ρ_{mn} are the mass coefficients related to the porosity ϕ and the mass densities ρ_s and ρ_f of the solid, and fluid ρ_{12} is the mass coupling. ρ_{12} is related to dynamic tortuosity, $\overline{\rho_{12}} = \phi \cdot \rho_f[1 - \alpha_\infty] - \frac{Z}{\sqrt{i \cdot \omega}}$, where $Z = \frac{2 \cdot \phi}{\Lambda}\sqrt{\rho_f \cdot \eta}$, Λ is the viscous characteristic length, and α_∞ is the dynamic tortuosity.[69] For a variety of smooth pore shapes, the relationship between viscous characteristic length Λ and the pore form factor M can be represented by $M = \frac{8\alpha_\infty k_0}{\Lambda^2 \phi}$.[66] The parameter $b = \frac{\eta \phi^2}{\mathcal{K}}$ serves as a dissipation factor and is a function of the porosity ϕ.

The Fourier transform solution of velocities for the shear wave (c_T^*) and longitude wave (c_{L1}^* and c_{L2}^*) in solid–liquid two-phase porous media with viscous losses can be expressed as follows:[70]

$$\begin{aligned} c_T^{*2} &= N\left(\rho_{22} + \frac{b}{i\omega}\right) \Big/ \left[\left(\rho_{11} + \frac{b}{i\omega}\right)\left(\rho_{22} + \frac{b}{i\omega}\right) - \left(\rho_{12} - \frac{b}{i\omega}\right)^2\right] \\ &= N\rho_{22}(\omega)/[\rho_{11}(\omega)\rho_{22}(\omega) - \rho_{12}^2(\omega)], \end{aligned} \tag{4}$$

$$c_{Lj}^{*2} = \frac{\left(M + \frac{b}{i\omega}H\right) \pm \sqrt{\left(M + \frac{b}{i\omega}H\right)^2 - 4L\left(\rho_{11}\rho_{22} - \rho_{12}^2 + \frac{b}{i\omega}\rho\right)}}{2\left(\rho_{11}\rho_{22} - \rho_{12}^2 + \frac{b}{i\omega}\rho\right)}, \quad (j = 1,2), \tag{5}$$

where the elastic coefficient $N = \mu_b$, $\rho_{11}(\omega) = \rho_{11} + \frac{b}{i\omega}$, $\rho_{12}(\omega) = \rho_{12} - \frac{b}{i\omega}$, $\rho_{22}(\omega) = \rho_{22} + \frac{b}{i\omega}$, $H = (P + R + 2Q)$, $L = (PR - Q^2)$, $M = (R\rho_{11} + P\rho_{22} - 2Q\rho_{12})$, $\rho = \rho_{11} + \rho_{22} + 2\rho_{12}$, and ω denotes the angular frequency.

The velocity of shear wave (c_T) and two types of longitude wave (c_{L1} and c_{L2}) in solid–liquid two-phase porous media without viscosity is given by[54,55]

$$c_T^2 = N\rho_{22}/(\rho_{11}\rho_{22} - \rho_{12}^2), \tag{6}$$

$$c_{Lj}^2 = \frac{M \pm \sqrt{M^2 - 4L(\rho_{11}\rho_{22} - \rho_{12}^2)}}{2(\rho_{11}\rho_{22} - \rho_{12}^2)}, \quad (j = 1,2). \tag{7}$$

By comparing the velocities in solid–liquid two-phase porous media with and without viscosity, we observe that the viscosity loss alters Biot's mass coefficients ρ_{mn} into complex quantities. This results in the shear wave velocity and yields the fast and slow longitudinal wave velocities that are complex numbers. As sound waves propagate through a dissipative solid–liquid two-phase porous medium, their amplitudes decay progressively with increased propagation distance.

To account for high-frequency dissipation, Biot's mass coefficients can be transformed as follows:

$$\rho_{mn}(\omega) = \rho_{mn} + (-1)^{m+n}\frac{bF(\kappa)}{i\omega}, \quad (m, n = 1,2). \tag{8}$$

where $F(\kappa) = \frac{1}{3}\frac{i^{1/2}\kappa \tanh(i^{1/2}\kappa)}{1 - \frac{1}{i^{1/2}\kappa}\tanh(i^{1/2}\kappa)}$ is a complex number that represents the deviation from Poiseuille's law as frequency increases, reflecting the phase difference between velocity and friction forces.[54] The frequency-dependent dissipation coefficient $\kappa = a\left(\frac{2\pi f \rho_f}{\eta}\right)^{\frac{1}{2}}$, where a is the average pore size in the porous medium.

The attenuation coefficients are determined by the imaginary parts of the complex wave numbers:

$$\alpha_T^* = -\mathrm{Im}(k) = -\mathrm{Im}\left(\frac{2\pi f}{c_T^*}\right), \tag{9}$$

$$\alpha_{Lj}^* = -\mathrm{Im}(k) = -\mathrm{Im}\left(\frac{2\pi f}{c_{Lj}^*}\right), \quad (j = 1,2). \tag{10}$$

The high-frequency dissipation coefficient α^* is influenced by several factors, including the porosity ϕ, the average pore size a of the solid–liquid two-phase porous medium, the frequency f

Table 1 Structural and acoustic parameters of cancellous bone.[66]

Parameters	Value
Young's modulus of solid bone E_s	22 GPa
Poisson's ratio of solid bone v_s	0.32
Poisson's ratio of skeletal frame v_b	0.32
Compressibility modulus of the solid κ_s	20.37 GPa
Solid density ρ_s	1960 kg/m^3
Fluid density ρ_f	1000 kg/m^3
Compressibility modulus of the solid κ_f	2.28 GPa
Fluid viscosity η_f	0.001 Pa · s
Power index n	$n(\theta) = 1.43\cos^2(\theta) + 2.14\sin^2(\theta)$
Tortuosity α_∞	$\alpha_\infty = 1 - 0.259\left(1 - \frac{1}{\phi}\right) + 0.864\cos^2(\theta)$
Pore size a	1 mm
Form factor M	4

Table 2 Permeability of different porosities.[71,72]

Porosity ϕ	Permeability k_0 (m^2)
0.72	5×10^{-9}
0.75	7×10^{-9}
0.80	2×10^{-8}
0.83	3×10^{-8}
0.90	8×10^{-8}

of the acoustic wave, and the fluid viscosity η. Therefore, the porosity ϕ of cancellous bone can be inferred based on the frequency-dependent attenuation coefficient.

3 Numerical Simulations

3.1 Numerical Simulation Parameters

Based on the above modified Biot's theory, we numerically simulated the propagation of acoustic waves in porous cancellous bone using MATLAB (version R2020b, MathWorks, Natick, Massachusetts, United States). The parameters used for these simulations are listed in Tables 1 and 2. It should be noted that, in general, the porosity of normal cancellous bone is ~0.73,[73,74] and that of osteoporotic cancellous is larger than this value. Therefore, we mainly conducted research using the porosity range of 0.72 to 0.90. We specifically examined the influences of porosity and sound frequency on sound velocity and attenuation.

3.2 Numerical Simulation Results

Based on the modified Biot's theory outlined above, we establish a computational model of semi-infinite cancellous bone and numerically simulate the propagation of PA waves in cancellous bone generated by bone marrow on the bone surface irradiated by a pulsed spotlight with a diameter of 2 mm. Figures 1(a) and 1(b) demonstrate the PA field at 17.92 μs in the cancellous bone with 0.72 and 0.83 porosity, respectively, including fast longitude wave (fast P wave), slow

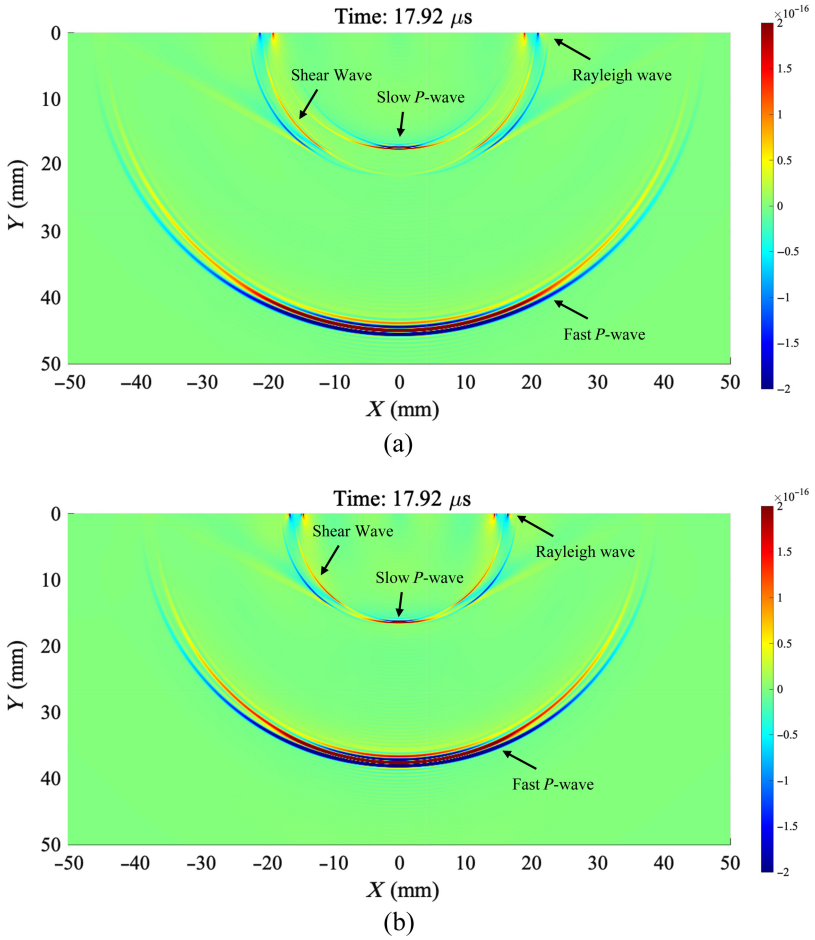

Fig. 1 Numerical simulation results of the sound field of PA wave generated by photoexcited bone marrow clusters on the boundary of semi-infinite cancellous bone propagating in cancellous bone with porosities of (a) 0.72 and (b) 0.83 at 17.92 μs (Video 1, mp4, 3.165 MB [URL: https://doi.org/10.1117/1.JBO.29.S1.S11526.s1]; Video 2, mp4, 3.094 MB [URL: https://doi.org/10.1117/1.JBO.29.S1.S11526.s2]).

longitude wave (slow P wave), shear wave, and Rayleigh waves (for the complete 0 to 17.92 μs sound field simulation, see Video 1 for a porosity of 0.72 and Video 2 for a porosity of 0.83). The numerical simulation shows that the speed and amplitude of fast P waves are much larger than those of other wave modes and other wave modes, which means that we can extract very clean fast P waves from the PA signal in the time domain.

Figures 2(a) and 2(b) illustrate the calculated trend of the velocity of fast and slow P waves propagating in solid–liquid two-phase porous media with porosity and frequency, respectively. Similarly, in the calculated porosity range of 0.72 to 0.90, the velocity of fast P wave (c_f) is much higher than that of slow P wave (c_s) at the same porosity. Notably, both fast and slow P wave velocities are insensitive to frequency change, that is, there is almost no dispersion, which is very advantageous for PA detection because the bandwidth of the PA signal is usually broad. However, both velocities decrease significantly with increasing porosity, which is also consistent with Fig. 1. This is mainly because the fact that as the porosity increases, the proportion of the solid phase decreases and the solid–liquid coupling becomes weaker, leading to a decrease in the velocity of the fast and slow waves, respectively.

Figures 3(a) and 3(b) showcase the viscous absorption attenuation coefficients for fast and slow P waves as they travel through solid–liquid two-phase porous media, respectively. In the calculated porosity range of 0.72 to 0.90, the absorption attenuation coefficient for the fast P wave is much smaller than that of the slow P wave with the same porosity. In addition, these attenuation coefficients are influenced by both the porosity of the cancellous bone and the

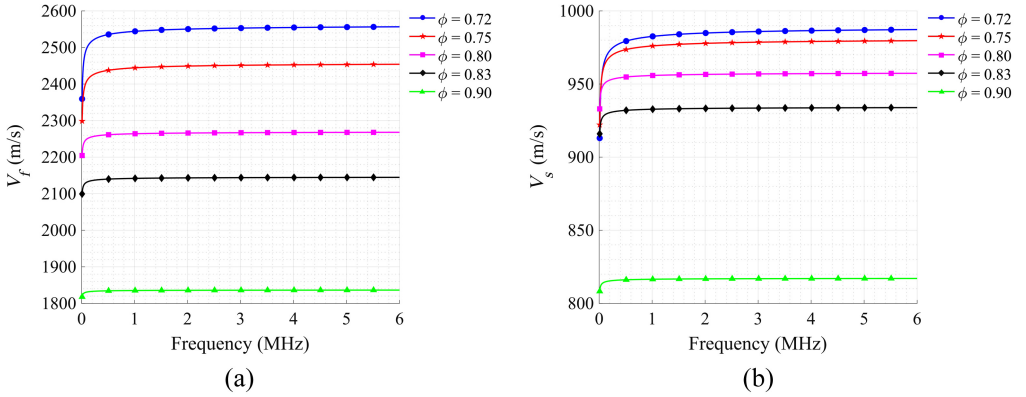

Fig. 2 Numerical simulation results. SoS of (a) fast and (b) slow longitude waves as a function of frequency at different porosities.

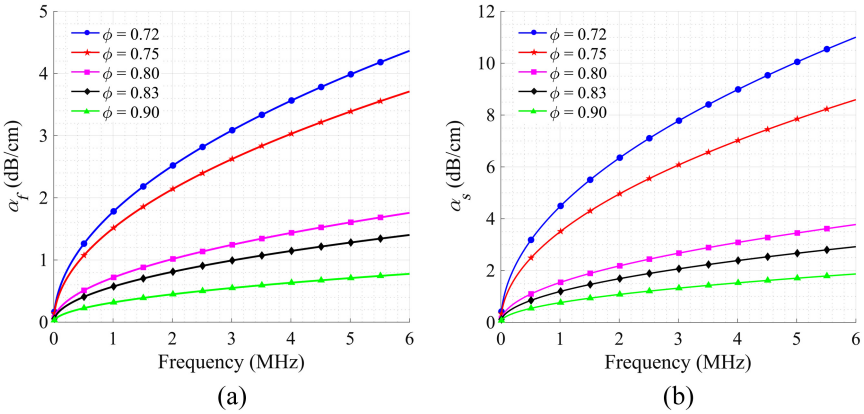

Fig. 3 Numerical simulation results. Viscous absorption attenuation coefficients of (a) fast and (b) slow longitude waves as a function of frequency at different porosities.

frequency of the acoustic waves. When the porosity is constant, the absorption attenuation coefficients for both fast and slow waves increase with increasing frequency. The attenuation coefficients exhibit a shift from fast to slow changes, eventually tending toward a linear pattern within the frequency range of 1 to 6 MHz as the frequency increases. Conversely, when the frequency is held constant, the absorption attenuation coefficient decreases as the porosity increases. This is mainly because as the porosity of cancellous bone increases, the solid–liquid interface area decreases, which in turn leads to a reduction in energy dissipation caused by the relative motion between the solid bone trabecular frame and the liquid bone marrow.

These simulation results indicate that the fast P wave with high speed and low attenuation is more suitable for the PA detection of cancellous bone, and the porosity ϕ of porous media can be evaluated based on the attenuation of acoustic waves across various frequencies.

4 PA-DAS Method

As discussed earlier, the PA signal arriving at the transducers is a complex mixture of broadband signals originating from distributed PA sources and the inherent acoustic propagation characteristics of porous cancellous bone. The relationship of PA signals received by the transducers, $p_1(t_1)$ and $p_2(t_2)$, in the time domain, can be represented as

$$p_2(t_2) = p_1(t_1) \otimes h(t_2 - t_1), \tag{11}$$

where $\otimes$ denotes the convolution operator, $p_1(t_1)$ represents the PA signal generated by bone tissue at time t_1, and $p_2(t_2)$ represents the PA signal after propagation of the cancellous bone.

And t_1 is any time point in p_1, t_2 is the corresponding time point of t_1 in p_2 after propagation, $t_2 - t_1$ represents the propagation time of the signal in the system. $h(t)$ denotes the system impulse response of bone tissue. Applying the Fourier transform to Eq. (11) yields the spectrum of PA signals arriving at the transducers:

$$P_2(\omega) = P_1(\omega)H(\omega)e^{j\omega(t_2-t_1)}, \tag{12}$$

where $P_1(\omega)$ and $P_2(\omega)$ denote the Fourier transforms of $p_1(t_1)$ and $p_2(t_2)$, respectively, and $H(\omega)$ is the Fourier transform of $h(t_2 - t_1)$. We can derive the frequency-related acoustic propagation characteristics of cancellous bone by calculating the differential attenuation spectrum of the signal after propagation and the PA signal generated by sources:

$$H(\omega) = \frac{|P_2(\omega)|}{|P_1(\omega)|}. \tag{13}$$

Figure 3 shows that the attenuation coefficient is approximately linear within the 1 to 6 MHz range. Thus the acoustic propagation characteristics within this frequency band can be linearly fitted to quantify attenuation across different frequencies.

5 *Ex vivo* Experiments on Rabbit Bone Specimens

Based on the results of theoretical and numerical simulations, the PA experiment was conducted on a rabbit osteoporosis model to verify the feasibility of bone evaluation based on PA-DAS.

5.1 Animal Model and Bone Tissue Sample

In our study, we used a sample of eleven 5-month-old female New Zealand white rabbits. Six were randomly selected to undergo ovariectomy, forming the experimental group, while the remaining five received a sham operation to serve as the control group. After 5 months of identical living conditions, all rabbits were euthanized. The left metaphyseal region was then carefully dissected and sectioned into slices with a uniform thickness of 1.5 mm. Dense peripheral bone tissue was removed, and the slices were further trimmed to a standard width D_b equal to 10 mm, as shown in Fig. 4(a), making them suitable for the PA experiments.

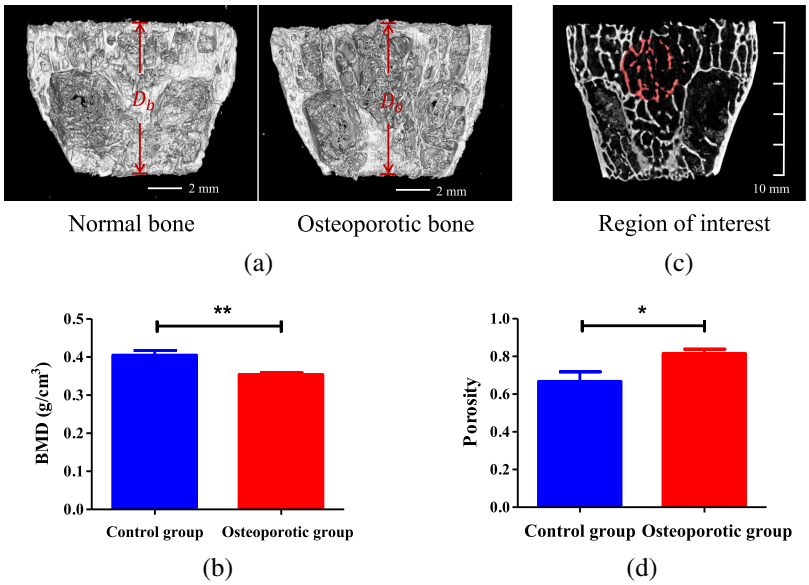

Fig. 4 Micro-CT results: (a) 3D images of normal bone and osteoporotic bone. (b) Statistical analysis results of BMD of bone specimens from the osteoporotic group ($n = 6$) and control group ($n = 5$) (**$p < 0.01$). (c) ROI used to calculate porosity. (d) Statistical analysis results of porosity of bone specimens from the osteoporotic groups ($n = 6$) and control group ($n = 5$) (*$p < 0.05$).

5.2 Gold Standard-BMD

Following the PA experiments, all eleven bone samples from both the experimental and control groups were subjected to microcomputed tomography scanning (Micro-CT, venus001, Avatar3, Pingsheng Life Medical Technology, Shanghai, China). Three-dimensional images of both the osteoporotic and normal bones are presented in Fig. 4(a). As evidenced by Fig. 4(b), the BMD of the normal bones in the control group was significantly higher than that of the osteoporotic bones in the experimental group ($p < 0.01$). In Fig. 4(d), the statistical analysis of the region of interest (ROI) from Fig. 4(c) reveals a significantly higher porosity in the osteoporotic group compared with the control group ($p < 0.05$). Literature suggests that higher BMD is inversely related to porosity.[73–77] Therefore, it can be concluded that osteoporotic bone exhibits higher porosity compared with normal bone.

5.3 PA Experimental Setup

To measure the frequency-dependent attenuation of PA signals in cancellous bone, we propose an eccentric excitation differential detection system specifically for PA experiments. Figure 5 illustrates the schematic layout of the experimental setup. A tunable optical parametric oscillator laser (Phocus Mobile, OPOTEK, Carlsbad, California, United States) produces laser pulses with durations ranging from 2 to 5 ns. We selected a laser wavelength of 1730 nm, which corresponds to the significant specific absorption wavelength of lipids[78,79]—a major component of bone marrow clusters[80]—to irradiate the bone samples and thereby excite PA signals.[81,82] To compensate for variations in laser energy over time, a spectrophotometer with a 9:1 transmittance-to-reflectance ratio was used to split the laser beam into two paths. One path was focused using a convex lens to irradiate a blackbody, and the other was weakly focused on one side of the bone tissue sample surface, tangent to the side of the sample, forming a light spot with a diameter D_l of ~2 mm. The bone sample was placed on a 5 cm thick phantom to mitigate any direct light or sound reflections from the platform. As shown in Fig. 5, a needle hydrophone T1 (HNC1500, ONDA Corporation, Sunnyvale, California, United States) with a bandwidth of 0 to 20 MHz was placed on the side of the sample near the light spot to receive the unattenuated PA signals. These signals were then amplified by 25 dB using an amplifier (5072PR, Olympus Corporation, Tokyo, Japan) and subjected to 1 MHz high-pass filtering to remove low-frequency noise. On the opposite side of the light source, a planar transducer with a center frequency of 2.25 MHz (Olympus Corporation, Tokyo, Japan) was positioned to receive the PA signals transmitted through the cancellous bone. These signals were amplified by another 25 dB using an amplifier (5073PR, Olympus Corporation, Tokyo, Japan). Both transducers were acoustically coupled to the bone sample using a transparent ultrasonic coupling agent. Concurrently, a 1 MHz focusing transducer (Olympus Corporation, Tokyo, Japan) was employed to receive the PA signal generated by the blackbody. Data acquisition was performed using a digital oscilloscope (HDO6000, Teledyne Lecroy, United States) set at a sampling rate of 250 MHz, which was deemed sufficient for our experimental requirements. Due to the anisotropic properties of cancellous bone, we employed a translation stage to move the bone sample longitudinally in 2 mm increments, for a total of three. This enabled us to capture PA signals at four distinct positions, thus providing a comprehensive

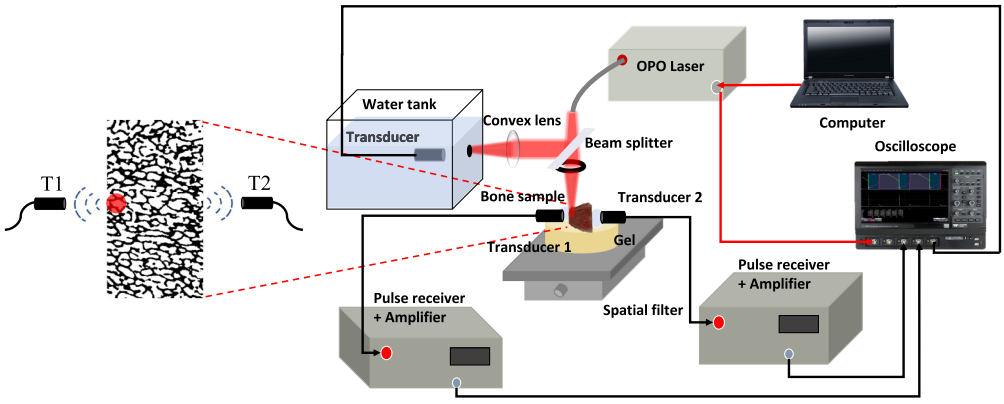

Fig. 5 Schematic of experimental setup for PA measurements of bone samples.

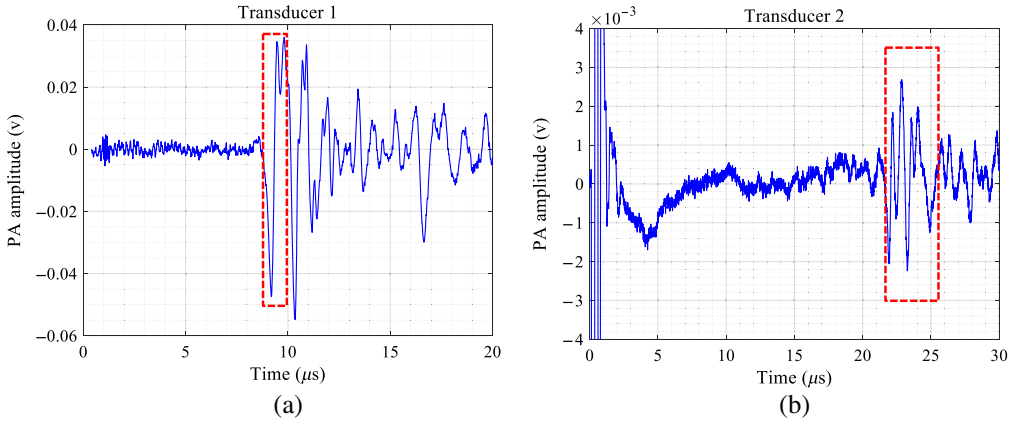

Fig. 6 PA signals generated by bones received by (a) the transducer near the light source T1 and (b) the transducer away from the light source T2.

evaluation of signal attenuation throughout the cancellous bone. To improve the signal-to-noise ratio, PA signals were recorded 50 times at each position and subsequently averaged.

5.4 PA Signal Processing

As shown in Fig. 5, the PA signal received by the hydrophone T1 closest to the light source serves as the unattenuated signal generated by the cancellous bone. Conversely, the PA signal received by transducer T2 located farther from the light source is a composite, reflecting both the inherent properties of the PA source and the acoustic propagation medium. By calculating the PA-DAS for both transducers, we can isolate and understand the frequency-related propagation characteristics specific to cancellous bone.

In the experiment, only longitudinal wave signals could be picked up because the gel was used as coupling agent. Moreover, the numerical results in Sec. 3.2 show that the attenuation of the slow *P* wave is much greater than that of the fast *P* wave, and the speed is much smaller than that of the fast *P* wave. Therefore, it is more meaningful to analyze the fast *P* wave signals with low attenuation than the complete signal.

It is necessary to select a reasonable time window for more accurate spectral analysis. Thus we introduce the SoS for bone marrow $c_m = 1500$ m/s, which is larger than slow *P* wave and smaller than fast *P* wave, and bone trabecular $c_t = 3200$ m/s (Ref. 66), which is larger than fast *P* wave, to calculate the start and end time of the picking window for fast-wave signals. As delineated by the red dotted box in Fig. 6(a), the direct PA signal duration for T1 is given by $t1 = \frac{D_l}{c_m} = 1.33$ μs. The earliest and latest times for the PA signal of T2 were selected by $\frac{D_b - D_l}{c_t}$, and $\frac{D_b}{c_m}$, respectively. The length of the PA signal as captured by T2 is $t2 = \frac{D_b}{c_m} - \frac{D_b - D_l}{c_t} = 4.17$ μs.

The frequency–response curve of the transducer T2, centered at 2.25 MHz, is presented in Fig. 7(a). As evident in this curve, the transducer produces its maximum output at the central

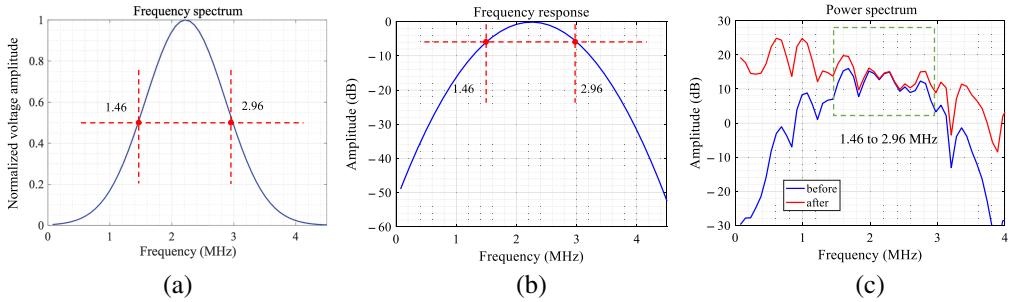

Fig. 7 (a) Frequency–response curve of T2 provided by the Olympus Corporation (Tokyo, Japan). (a) Frequency–response curve of T2. Red intersection point denotes the frequency corresponding to the maximum value decreasing by 6 dB. (b) Spectrum of the PA signal of bone received by T2 (solid blue line) and spectrum after frequency–response correction (solid red line).

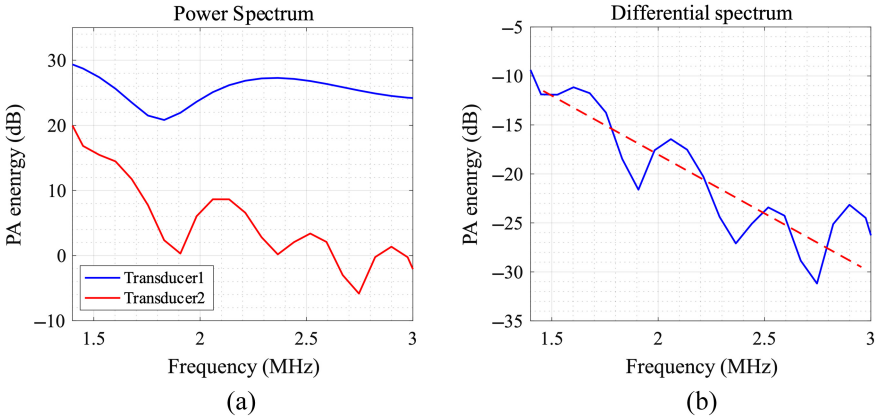

Fig. 8 (a) Spectrum of PA signals received by the two transducers. (b) Differential spectrum of PA signal received by the two transducers.

frequency of 2.25 MHz and attenuates on either side, leading to distortion in the frequency domain of the PA signal as displayed by the oscilloscope. To more accurately investigate the spectral characteristics of the PA signal, it is necessary to correct the observed output signals in line with the frequency–response curve of the transducer. Corresponding to a 6 dB decline from the maximum frequency response to prevent excessive correction of high-frequency noise, a fitting frequency band ranging from 1.46 to 2.96 MHz was selected. After applying a 1 MHz high-pass filter to eliminate the influence of low-frequency noise, the spectral characteristics of the PA signal received by the distant transducer—both before and after minus the frequency response of transducer T2 for correction based on the frequency response provided by the Olympus Corporation (Tokyo, Japan)—are illustrated by the blue and red curves in Fig. 7(b). Although the frequency–response curve of the broadband hydrophone T1 is uniform, the signals received by T1 do not need correction. Given the data in Fig. 3, the linear fitting for the frequency curve was confined to the 1.46 to 2.96 MHz range.

To account for the spectral differences of the PA source caused by the anisotropy of cancellous bone, we calculated the PA-DAS $\mathrm{As}(f)$ based on Eq. (14) to evaluate the acoustic propagation characteristics of the bone:

$$\mathrm{As}(f) = 10\ \mathrm{lg}\left(\frac{\mathrm{PSD}_2(f)}{\mathrm{PSD}_1(f)}\right). \tag{14}$$

Here PSD_1 and PSD_2 represent the power spectra of PA signals received by transducers 1 and 2, respectively, as depicted in Fig. 8(a). Notably, the PA signal from the transducer closer to the light source includes a higher concentration of high-frequency components due to the absence of propagation attenuation. In contrast, the PA signal from the transducer situated farther from the light source was mainly composed of low-frequency components owing to significant propagation attenuation in cancellous bone.

Linear fitting was performed for the PA-DAS in the frequency range of 1.46 to 2.96 MHz. From this, we extracted the absolute value of slope—slope—as a quantization parameter, enabling us to obtain the frequency-related attenuation of the PA signal as it travels through the bone.

5.5 Results

Figure 9 presents the slopes for both normal and osteoporotic bones, revealing a significantly lower slope for osteoporotic bones when compared with normal ones ($^{**}p < 0.01$). The average slope of the normal group is 8.77 dB/cm/MHz and the osteoporosis is 2.55 dB/cm/MHz. The attenuation coefficient of trabecular bone given in literature is 9.94 dB/cm/MHz.[83] Ignoring the attenuation of bone marrow, the attenuation coefficients of cancellous bone with porosity ϕ can be calculated by $9.94 \times (1 - \phi)$ dB/cm/MHz. It is the same order of magnitude as our experimental results but lower due to the ignorance of bone marrow attenuation and scattering attenuation, proving the rationality of our experiment design and implementation. Given that normal bone has higher BMD and lower porosity, the attenuation of high-frequency components is

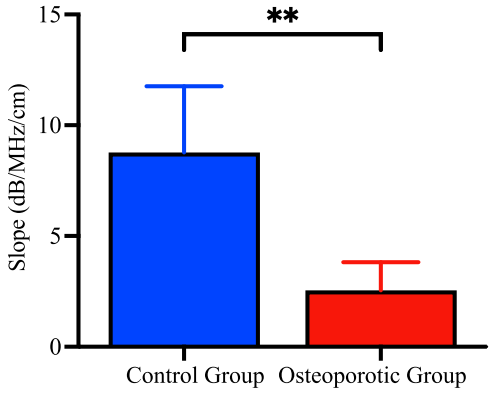

Fig. 9 Statistical results of bone slope in the two studied groups (**$p < 0.01$).

stronger during PA signal propagation through the cancellous bone structure. This results in a decreased high-to-low frequency ratio in the spectral distribution, leading to a larger slope for the control group. Conversely, osteoporotic bones have a slower slope, due to the weakening of the solid–liquid interface coupling and the decrease of viscosity attenuation caused by lower BMD and higher porosity. The experimental results qualitatively agree with the numerical simulation outcomes, quantitative comparisons are discussed in Sec. 6.

6 Conclusion and Discussion

PA technology holds immense promise for bone assessment and imaging. Researchers have proposed various spectral analysis methods in PA bone assessment, such as physicochemical[44] and time-frequency spectrum,[84,85] to discern characteristics of the bone microstructure and chemical composition of bone. However, achieving high-precision PAI to visualize the distribution of bone marrow clusters in the bone remains challenging due to the ultrawideband spectrum (from 220 kHz to 13.5 MHz in cancellous bone, see Appendix A2 in the Supplementary Material) and high frequency of PA signals generated by cancellous bone. Comprehending the attenuation of PA signals in cancellous bone is a pivotal cornerstone for high-resolution PAI of cancellous bone. The propagation of PA waves generated by bone marrow (mainly lipids) through the cancellous bone, a solid–liquid two-phase porous medium was studied theoretically, numerically, and experimentally in this study. Biot's theory was modified to account for high frequencies and viscosity, providing an analytical solution for the broadband PA signal's behavior in cancellous bone. Numerical simulation results show that when porosity is greater than 0.72, the viscous absorption attenuation of PA signals increases with frequency but decreases with greater porosity. Additionally, the fast *P* wave with high speed and low attenuation is more suitable for the detection of cancellous bone. In PA detection, to isolate the acoustic propagation properties of porous cancellous bone from the aliasing with the PA source, a PA-DAS method was proposed and a parameter slope was extracted to quantify frequency-specific acoustic attenuation. Experimental data on a rabbit osteoporotic model demonstrate that PA-DAS can effectively distinguish normal from osteoporotic bone, validating its utility for bone evaluation.

As shown in Fig. 9, the average slope of the normal group measured 8.77 dB/cm/MHz, and the osteoporosis group exhibited a slope of 2.55 dB/cm/MHz. Nevertheless, the slopes obtained from numerical simulations were 0.61 dB/cm/MHz for the normal bone and 0.19 dB/cm/MHz for the osteoporosis bone, as detailed in Appendix A1 in the Supplementary Material. Although the qualitative agreement between the experimental and simulated results is evident, quantitative disparities still exist. This is because cancellous bone's acoustic propagation properties are predominantly governed by absorption and scattering of viscous solid–liquid two-phase porous structure.[86] Absorption attenuation is an energy dissipation process caused by viscous friction at the fluid–solid interface, whereas scattering attenuation[87] arises from reflections and scattering due to acoustic disparities between solid trabecular bone and liquid bone marrow, leading to the reduction of acoustic energy along the original propagation direction.[88] This study focused on high-frequency viscous absorption attenuation in porous media, refining Biot's theory to address

higher frequency bands in PA signals and the viscosity of bone marrow. However, for more accurate quantification of scattering characteristics of cancellous bone, future studies should consider the anisotropy and heterogeneity intrinsic to its structure. Thankfully, the scattering attenuation in cancellous bone also adheres to a linear law with frequency.[87,89] The proposed method PA-DAS in this paper can be readily extended due to this approximation.

When considering the clinical applications of PA-DAS, it is crucial to account for the layers of cortical bone and soft tissue that envelop cancellous bone. As the transducers are located on opposite sides of the bone, the thickness of the dense bone and soft tissue on both sides of the bone should be considered. Our previous studies successfully isolated PA signals originating from soft tissue, cortical bone, and cancellous bone in the time domain.[45] Using the SoS to calculate the thickness of these three types of media and employing the exponential attenuation law to consider the optical and ultrasonic propagation attenuation of cortical bone and soft tissue, we can compensate the PA signals in further studies to isolate and analyze the pure PA signal corresponding to cancellous bone.[90–92] In addition, the diameter of calcaneus bone in the human body is in the range of 2 to 3 cm.[43] The attenuation of the cancellous bone to the high-frequency PA signal is stronger, and the received signal is mainly concentrated in the lower frequency band between 220 kHz and 1 MHz. According to the numerical simulation results shown in Fig. 3, the relationship between the attenuation coefficient and frequency is nonlinear at frequencies lower than 1 MHz. Therefore, it is necessary to fit the variation of low-frequency attenuation coefficient with frequency using a nonlinear function before applying this method to clinical practice.

Disclosures

The authors have no relevant financial interests in the manuscript and no other potential conflicts of interest to disclose.

Code and Data Availability

The data that support the findings of this article are not publicly available due to privacy. The code can be requested from the author at q.cheng@tongji.edu.cn

Author Contributions

Wenyi Xu and Weiya Xie contributed equally to this paper. Wenyi Xu and Weiya Xie contributed to the theory, simulations, design and operation of the experiments, and the analysis of data and drafted the manuscript. Dong Yu contributed to the design of experiments. Haohan Sun, Ying Gu, and Xingliang Tao contributed to the operation of experiments. Menglu Qian contributed to the theory revision and manuscript revision. Liming Cheng checked the experimental proposal. Hao Wang contributed to the theory and the numerical simulations. Qian Cheng presided over the creative execution and promotion of the study, as well as an overall check of the manuscript.

Acknowledgments

This project was supported by the National Natural Science Foundation of China (Grant Nos. 12034015 and 11827808), Shanghai Academic Research Leader Program (Grant No. 21XD1403600), Shanghai Municipal Science and Technology Major Project (Grant No. 2021SHZDZX0100), and the Postdoctoral Science Foundation of China (Grant No. 2019M65156). We would like to thank Editage for English language editing.

References

1. S. R. Cummings and L. J. Melton, "Epidemiology and outcomes of osteoporotic fractures," *Lancet* **359**(9319), 1761–1767 (2002).
2. J. Y. Reginster and N. Burlet, "Osteoporosis: a still increasing prevalence," *Bone* **38**(2 Suppl. 1), S4–S9 (2006).
3. J. J. Jolly et al., "Protective effects of selected botanical agents on bone," *Int. J. Environ. Res. Public Health* **15**(5), 963 (2018).
4. C. Cooper, G. Campion, and L. J. Melton, "Hip fractures in the elderly: a world-wide projection," *Osteoporosis Int.* **2**(6), 285–289 (1992).

5. K. A. Wear, "Mechanisms of interaction of ultrasound with cancellous bone: a review," *IEEE Trans. Ultrason. Ferroelectr. Freq. Control* **67**(3), 454–482 (2020).
6. E. Seeman, "Age- and menopause-related bone loss compromise cortical and trabecular microstructure," *J. Gerontol. A Biol. Sci. Med. Sci.* **68**(10), 1218–1225 (2013).
7. A. Vesterby, H. J. Gundersen, and F. Melsen, "Star volume of marrow space and trabeculae of the first lumbar vertebra: sampling efficiency and biological variation," *Bone* **10**(1), 7–13 (1989).
8. J. F. Griffith, "Age-related changes in the bone marrow," *Curr. Radiol. Rep.* **5**(6), 24 (2017).
9. P. Pisani et al., "Screening and early diagnosis of osteoporosis through X-ray and ultrasound based techniques," *World J. Radiol.* **5**(11), 398–410 (2013).
10. J. A. Kanis, "Assessment of fracture risk and its application to screening for postmenopausal osteoporosis: synopsis of a WHO report," *Osteoporosis Int.* **4**, 368–381 (1994).
11. C. V. Albanese, F. De Terlizzi, and R. Passariello, "Quantitative ultrasound of the phalanges and DXA of the lumbar spine and proximal femur in evaluating the risk of osteoporotic vertebral fracture in postmenopausal women," *Radiol. Med.* **116**(1), 92–101 (2011).
12. C. F. Njeh, C. M. Boivin, and C. M. Langton, "The role of ultrasound in the assessment of osteoporosis: a review," *Osteoporosis Int.* **7**(1), 7–22 (1997).
13. S. R. Cummings et al., "Risk factors for hip fracture in white women. Study of Osteoporotic Fractures Research Group," *N. Engl. J. Med.* **332**(12), 767–773 (1995).
14. C. C. Glüer et al., "Three quantitative ultrasound parameters reflect bone structure," *Calcif. Tissue Int.* **55**(1), 46–52 (1994).
15. J. E. Adams, "Quantitative computed tomography," *Eur. J. Radiol.* **71**(3), 415–424 (2009).
16. X. S. Liu et al., "Bone density, geometry, microstructure, and stiffness: relationships between peripheral and central skeletal sites assessed by DXA, HR-pQCT, and cQCT in premenopausal women," *J. Bone Miner. Res.* **25**(10), 2229–2238 (2010).
17. C. S. Gee et al., "Validation of bone marrow fat quantification in the presence of trabecular bone using MRI," *J. Magn. Reson. Imaging* **42**(2), 539–544 (2015).
18. H. Yu et al., "Multiecho reconstruction for simultaneous water-fat decomposition and T_2* estimation," *J. Magn. Reson. Imaging* **26**(4), 1153–1161 (2007).
19. H. Yu et al., "Field map estimation with a region growing scheme for iterative 3-point water-fat decomposition," *Magn. Reson. Med.* **54**(4), 1032–1039 (2005).
20. J. F. Griffith et al., "Vertebral bone mineral density, marrow perfusion, and fat content in healthy men and men with osteoporosis: dynamic contrast-enhanced MR imaging and MR spectroscopy," *Radiology* **236**(3), 945–951 (2005).
21. J. F. Griffith et al., "Vertebral marrow fat content and diffusion and perfusion indexes in women with varying bone density: MR evaluation," *Radiology* **241**(3), 831–838 (2006).
22. K. Y. Chin and S. Ima-Nirwana, "Calcaneal quantitative ultrasound as a determinant of bone health status: what properties of bone does it reflect?," *Int. J. Med. Sci.* **10**(12), 1778–1783 (2013).
23. M. Matsukawa, "Bone ultrasound," *Jpn. J. Appl. Phys.* **58**(SG), SG0802 (2019).
24. Q. Grimal and P. Laugier, "Quantitative ultrasound assessment of cortical bone properties beyond bone mineral density," *IRBM* **40**(1), 16–24 (2019).
25. D. Ta et al., "Measurement of the dispersion and attenuation of cylindrical ultrasonic guided waves in long bone," *Ultrasound Med. Biol.* **35**(4), 641–652 (2009).
26. Q. Grimal et al., "Quantitative ultrasound of cortical bone in the femoral neck predicts femur strength: results of a pilot study," *J. Bone Miner. Res.* **28**(2), 302–312 (2013).
27. J. J. Kaufman and T. A. Einhorn, "Perspectives: ultrasound assessment of bone," *J. Bone Miner. Res.* **8**(5), 517–525 (1993).
28. S. Huang et al., "Interstitial assessment of aggressive prostate cancer by physio-chemical photoacoustics: an ex vivo study with intact human prostates," *Med. Phys.* **45**, 4125–4132 (2018).
29. S. Mallidi et al., "Prediction of tumor recurrence and therapy monitoring using ultrasound-guided photoacoustic imaging," *Theranostics* **5**(3), 289–301 (2015).
30. R. Cao et al., "Functional and oxygen-metabolic photoacoustic microscopy of the awake mouse brain," *NeuroImage* **150**, 77–87 (2017).
31. J. T. Oh et al., "Three-dimensional imaging of skin melanoma in vivo by dual-wavelength photoacoustic microscopy," *J. Biomed. Opt.* **11**(3), 034032 (2006).
32. L. Z. Xiang and F. F. Zhou, "Photoacoustic imaging application in tumor diagnosis and treatment monitoring," *Key Eng. Mater.* **364–366**, 1100–1104 (2007).
33. B. Lashkari and A. Mandelis, "Coregistered photoacoustic and ultrasonic signatures of early bone density variations," *J. Biomed. Opt.* **19**(3), 036015 (2014).
34. L. Yang et al., "Photoacoustic and ultrasound imaging of cancellous bone tissue," *J. Biomed. Opt.* **20**(7), 076016 (2015).

35. L. Yang et al., "Bone composition diagnostics: photoacoustics versus ultrasound," *Int. J. Thermophys.* **36**(5-6), 862–867 (2015).
36. B. Lashkari, L. Yang, and A. Mandelis, "The application of backscattered ultrasound and photoacoustic signals for assessment of bone collagen and mineral contents," *Quantum Imaging Med. Surg.* **5**(1), 46–56 (2015).
37. X. Wang et al., "Photoacoustic measurement of bone health: a study for clinical feasibility," in *IEEE Int. Ultrasonics Symp. (IUS)*, IEEE, Tours, France, pp. 1–4 (2016).
38. T. Feng et al., "Characterization of bone microstructure using photoacoustic spectrum analysis," *Proc. SPIE* **9323**, 93234I (2015).
39. T. Feng et al., "Bone assessment via thermal photo-acoustic measurements," *Opt. Lett.* **40**(8), 1721–1724 (2015).
40. T. Feng et al., "Functional photoacoustic and ultrasonic assessment of osteoporosis: a clinical feasibility study," *BME Front.* **2020**, 1081540 (2020).
41. I. Steinberg et al., "First-in-human study of bone pathologies using low-cost and compact dual-wavelength photoacoustic system," *IEEE J. Select. Top. Quantum Electron.* **25**(1), 1–8 (2019).
42. M. Weiss et al., "Reference database for bone speed of sound measurement by a novel quantitative multi-site ultrasound device," *Osteoporos. Int.* **11**(8), 688–696 (2000).
43. T. Feng et al., "The feasibility study of the transmission mode photoacoustic measurement of human calcaneus bone in vivo," *Photoacoustics* **23**, 100273 (2021).
44. T. Feng et al., "Characterization of multi-biomarkers for bone health assessment based on photoacoustic physicochemical analysis method," *Photoacoustics* **25**, 100320 (2022).
45. T. Feng et al., "Feasibility study for bone health assessment based on photoacoustic imaging method," *Chin. Opt. Lett.* **18**(12), 121704 (2020).
46. W. Xie et al., "Photoacoustic characterization of bone physico-chemical information," *Biomed. Opt. Express* **13**(5), 2668–2681 (2022).
47. W. Xie et al., "Bone microstructure evaluation by photoacoustic time-frequency spectral analysis," in *IEEE Int. Ultrasonics Symp. (IUS)*, IEEE, Las Vegas, Nevada, pp. 1–4 (2020).
48. E. A. Gonzalez and M. A. L. Bell, "Photoacoustic imaging and characterization of bone in medicine: overview, applications, and outlook," *Annu. Rev. Biomed. Eng.* **25**, 207–232 (2023).
49. Z. E. A. Fellah et al., "Ultrasonic wave propagation in human cancellous bone: application of Biot theory," *J. Acoust. Soc. Am.* **116**(1), 61–73 (2004).
50. M. A. Biot, "General theory of three-dimensional consolidation," *J. Appl. Phys.* **12**(2), 155–164 (1941).
51. M. A. Biot, "Theory of elasticity and consolidation for a porous anisotropic solid," *J. Appl. Phys.* **26**(2), 182–185 (1955).
52. M. A. Biot, "Theory of deformation of a porous viscoelastic anisotropic solid," *J. Appl. Phys.* **27**(5), 459–467 (1956).
53. M. A. Biot and D. G. Willis, "The elastic coefficients of the theory of consolidation," *J. Appl. Mech.* **24**(4), 594–601 (1957).
54. M. A. Biot, "Theory of propagation of elastic waves in a fluid-saturated porous solid. II. Higher frequency range," *J. Acoust. Soc. Am.* **28**(2), 179–191 (1956).
55. M. A. Biot, "Theory of propagation of elastic waves in a fluid-saturated porous solid. I. Low-frequency range," *J. Acoust. Soc. Am.* **28**(2), 168–178 (1956).
56. F. J. Fry and J. E. Barger, "Acoustical properties of the human skull," *J. Acoust. Soc. Am.* **63**(5), 1576–1590 (1978).
57. R. B. Ashman, J. D. Corin, and C. H. Turner, "Elastic properties of cancellous bone: measurement by an ultrasonic technique," *J. Biomech.* **20**(10), 979–986 (1987).
58. Z. A. Fellah et al., "Application of the Biot model to ultrasound in bone: direct problem," *IEEE Trans. Ultrason. Ferroelectr. Freq. Control* **55**(7), 1508–1515 (2008).
59. N. Sebaa et al., "Application of the Biot model to ultrasound in bone: inverse problem," *IEEE Trans. Ultrason. Ferroelectr. Freq. Control* **55**(7), 1516–1523 (2008).
60. M. Sadouki et al., "Ultrasonic propagation of reflected waves in cancellous bone: application of Biot theory," in *6th Eur. Symp. Ultrasonic Characterization of Bone*, IEEE, Corfu, Greece, pp. 1–4 (2015).
61. M. Pakula et al., "Application of Biot's theory to ultrasonic characterization of human cancellous bones: determination of structural, material, and mechanical properties," *J. Acoust. Soc. Am.* **123**(4), 2415–2423 (2008).
62. M. Hodaei, P. Maghoul, and N. Wu, "Three-dimensional biomechanical modeling of cylindrical bone-like porous materials subject to acoustic waves," *Int. J. Mech. Sci.* **213**, 106835 (2022).
63. M. R. J. Wyllie, G. H. F. Gardner, and A. R. Gregory, "Studies of elastic wave attenuation in porous media," *Geophysics* **27**(5), 569–589 (1962).
64. E. R. Hughes et al., "Ultrasonic propagation in cancellous bone: a new stratified model," *Ultrasound Med. Biol.* **25**(5), 811–821 (1999).

65. E. R. Hughes et al., "Estimation of critical and viscous frequencies for Biot theory in cancellous bone," *Ultrasonics* **41**(5), 365–368 (2003).
66. A. Bennamane and T. Boutkedjirt, "Theoretical and experimental study of the ultrasonic attenuation in bovine cancellous bone," *Appl. Acoust.* **115**, 50–60 (2017).
67. T. Cox et al., "k-space propagation models for acoustically heterogeneous media: application to biomedical photoacoustics," *J. Acoust. Soc. Am.* **121**(6), 3453–3464 (2007).
68. M. W. Sigrist and F. K. Kneubühl, "Laser-generated stress waves in liquids," *J. Acoust. Soc. Am.* **64**(6), 1652–1663 (1978).
69. D. L. Johnson, J. Koplik, and R. Dashen, "Theory of dynamic permeability and tortuosity in fluid-saturated porous media," *J. Fluid Mech.* **176**, 379–402 (1987).
70. T. Feng et al., "Photoacoustic bone characterization: a progress review," *Chin. Sci. Bull.* **68**(26), 3437–3454 (2023).
71. A. Hosokawa and T. Otani, "Ultrasonic wave propagation in bovine cancellous bone," *J. Acoust. Soc. Am.* **101**(1), 558–562 (1997).
72. M. L. McKelvie and S. B. Palmer, "The interaction of ultrasound with cancellous bone," *Phys. Med. Biol.* **36**(10), 1331–1340 (1991).
73. L. Cardoso et al., "In vitro acoustic waves propagation in human and bovine cancellous bone," *J. Bone Miner. Res.* **18**, 1803–1812 (2003).
74. D. Porrelli et al., "Trabecular bone porosity and pore size distribution in osteoporotic patients—a low field nuclear magnetic resonance and microcomputed tomography investigation," *J. Mech. Behav. Biomed. Mater.* **125**, 104933 (2022).
75. B. Li et al., "Characterization of a rabbit osteoporosis model induced by ovariectomy and glucocorticoid," *Acta Orthop.* **81**(3), 396–401 (2010).
76. A.W. Ebaerhardt, A.Y. Jones, and H. C. Blair, "Regional trabecular bone matrix degeneration and osteocyte death in femora of glucocorticoid treated rabbits," *Endocrinology* **142**(3), 1333–1340 (2001).
77. M. Hodaei and A. Mandelis, "Quantitative osteoporosis diagnosis of porous cancellous bone using poroelastodynamic modal analysis," *J. Acoust. Soc. Am.*, **154**, 3101–3124 (2023).
78. D.-K. Yao et al., "Photoacoustic measurement of the Grüneisen parameter of tissue," *J. Biomed. Opt.* **19**(1), 017007 (2014).
79. T. Feng et al., "Detection of collagen by multi-wavelength photoacoustic analysis as a biomarker for bone health assessment," *Photoacoustics* **24**, 100296 (2021).
80. G. Guglielmi and J. F. Griffith, "Bone marrow changes in osteoporosis," in *Osteoporosis and Bone Densitometry Measurements*, G. Guglielmi, Ed., pp. 69–85, Springer, Heidelberg, Berlin (2013)
81. H. W. Wang et al., "Label-free bond-selective imaging by listening to vibrationally excited molecules," *Phys. Rev. Lett.* **106**(23), 238106 (2011).
82. H. Lei et al., "Characterizing intestinal inflammation and fibrosis in Crohn's disease by photoacoustic imaging: feasibility study," *Biomed. Opt. Express* **7**(7), 2837–2848 (2016).
83. M. O. Culjat et al., "A review of tissue substitutes for ultrasound imaging," *Ultrasound Med. Biol.* **36**(6), 861–873 (2019).
84. W. Xie et al., "Wavelet transform-based photoacoustic time-frequency spectral analysis for bone assessment," *Photoacoustics* **22**, 100259 (2021).
85. W. Xu, W. Xie, and Q. Cheng, "Intelligent photoacoustic diagnosis of osteoporosis based on wavelet scattering network," in *IEEE Int. Ultrasonics Symp. (IUS)*, IEEE, Montreal, Québec, pp. 1–4 (2023).
86. P. Laugier, "Quantitative ultrasound of bone: looking ahead," *Joint Bone Spine* **73**(2), 125–128 (2006).
87. R. Strelitzki, P. H. F. Nicholson, and V. Paech, "A model for ultrasonic scattering in cancellous bone based on velocity fluctuations in a binary mixture," *Physiol. Meas.* **19**(2), 189–196 (1998).
88. M. F. Insana et al., "Describing small-scale structure in random media using pulse-echo ultrasound," *J. Acoust. Soc. Am.* **87**(1), 179–192 (1990).
89. C. M. Sehgal and J. F. Greenleaf, "Scattering of ultrasound by tissues," *Ultrasonic Imaging* **6**(1), 60–80 (1984).
90. A. Pifferi et al., "Optical biopsy of bone tissue: a step toward the diagnosis of bone pathologies," *J. Biomed. Opt.* **9**(3), 474–480 (2004).
91. C. Liu et al., "The analysis and compensation of cortical thickness effect on ultrasonic backscatter signals in cancellous bone," *J. Appl. Phys.* **116**(12), 124903 (2014).
92. M. Firbank et al., "Measurement of the optical properties of the skull in the wavelength range 650-950 nm," *Phys. Med. Biol.* **38**(4), 503–510 (1993).

Wenyi Xu is a PhD candidate from the Institute of Acoustics at the School of Physics Science and Engineering of Tongji University. She received her bachelor's degree from Tongji University in 2020. Her current research focuses on photoacoustic imaging and photoacoustic measurements of bone relevant research.

Weiya Xie received her PhD from the Institute of Acoustics at the School of Physics Science and Engineering of Tongji University in 2023. She received her bachelor's degree from Ocean University of China in 2017. Her current research focuses on photoacoustic measurement of bone health and photoacoustic imaging.

Dong Yu received her master's degree from the Institute of Acoustics at the School of Physics Science and Engineering of Tongji University in 2021. She received her bachelor's degree from Zhejiang Normal University in 2019.

Haohan Sun is a PhD student at the School of Physics Science and Engineering of Tongji University. He graduated from the School of Physics Science and Engineering of Tongji University with a bachelor of science degree in applied physics in 2022. His current research interests include acoustic non-line-of-sight imaging and the study of information complexity.

Ying Gu is a master's degree candidate from the Institute of Acoustics at the School of Physics Science and Engineering of Tongji University. She received her bachelor's degree from Suzhou University. Her current research focuses on underwater burial imaging.

Xingliang Tao is a master's degree candidate from the Institute of Acoustics at the School of Physics Science and Engineering of Tongji University. He received his bachelor degree in marine technology from the Ocean University of China in 2022. His current research interests include underwater optical visualization, turbulent flow, and hydrodynamic noise.

Menglu Qian is a professor at Tongji University. He received his BS degree in physics and his MS degree in acoustics from Tongji University in 1963 and 1981, respectively. He is the author of more than 200 journal papers and 2 books. His scientific research covers a wide range of fields of ultrasound, such as ultrasonic NDT, photoacoustics, laser ultrasonics, acoustic microscopy, acoustic cavitation and sonoluminescence, acousto-optic effect and sound field visualization, and medical ultrasound.

Liming Cheng is the president of Tongji Hospital and Director of Orthopedics at Tongji Hospital affiliated with Tongji University. He received his PhD from the Second Military Medical University. His research interests involved various aspects of clinical and basic research on spine and spinal cord injury.

Hao Wang is a lecturer at Tongji University. He received his BS degree in physics and his MS and PhD degrees in acoustics from Tongji University in 2001, 2004, and 2007, respectively. He is the author of more than 20 journal papers. His current research interests include ultrasonics simulation and inversion algorithms. He is a member of the ASC.

Qian Cheng is a professor at Tongji University. She received her BS degree in physics and her MS and PhD degrees in acoustics from Tongji University in 2000, 2003, and 2006, respectively. She is the author of more than 70 journal papers and 4 book chapters. Her current research interests include photoacoustics and ultrasonics. She is a member of SPIE, IEEE, and ASC.